# Combined Scattering, Interferometry and Fluorescence oblique illumination for live cell nanoscale imaging

**Yujie Zheng [1,2,ǂ], Yean Jin Lim [1,2,ǂ], Hanqi Lin[1,2], Tienan Xu[1,2], Carmen Longbottom [1,2], Viviane Delghingaro-Augusto[1], Yee Lin Thong [1], Christopher Parish[1], Elizabeth E Gardiner[1], Woei Ming Lee *[1,2,]**

[1] Division of Genomic Sciences and Cancer, The John Curtin School of Medical Research, The Australian National University, Canberra, ACT 2601, Australia

[2] ACRF INCITe Centre - ANU Node, The John Curtin School of Medical Research, The Australian National University, Canberra, ACT 2601, Australia

**Address for correspondence**
Dr W M Lee
The Australian National University,
Canberra ACT 2601, Australia
ǂ Equal contribution
*Email: steve.lee@anu.edu.au

**ABSTRACT** To determine the molecular and/or mechanical basis of cell migration using live cell imaging tools, it is necessary to correlate multiple 3D spatiotemporal events simultaneously. Fluorescence nanoscopy and label free nanoscale imaging can complement each other by providing both molecular specificity and structural dynamics of sub-cellular structure. In doing so, a combined imaging system would permit quantitative 3D spatial temporal detail of individual cellular components. In this paper, we empirically determined a series of optimal oblique scanning angles to achieve simultaneous label-free nanoscale imaging: interferometric scattering (iSCAT), rotational coherence scattering (ROCS) along with highly inclined, laminated optical sheet (HiLO) fluorescence imaging. The combined imaging capabilities of iSCAT, ROCS and HiLO enables (1) the identification of molecular targets (substrate or organelle), (2) quantification of 3D cell morphodynamics, and (3) tracking of intracellular organelles in 3D. This combined imaging tool was then used to characterize migrating platelets and adherent endothelial cells, both critical to the process of infection and wound healing. The combined imaging results of over ~1000 platelets, suggested that serum albumin (bovine) was necessary for platelets to migrate and scavenge fibrin/fibrinogen. Furthermore, we determine new asynchronous membrane fluctuations between the leading and rear edge of a migrating platelet. We further demonstrated that iSCAT, using oblique illumination, permitted the quantification of mitochondria dynamics on lung microvascular cells (HMVEC). Our data suggests that axial displacement of mitochondria is minimized when it is closer to the nucleus or the leading edge of a cell membrane that exhibits retrograde motion. Taken together, this combined imaging platform has proven to quantify multiple spatial temporal events of a migrating cell, that will undoubtedly open ways to new quantitative correlative nanoscale live cell imaging.

**Keywords:** Interferometry, Scattering, Fluorescence, Nanoscopy

## Introduction

Cells direct their movement through the coordination of extra- and intracellular nanoscale movements to fulfil their biological function in immune surveillance [1], wound healing [2, 3], clot formation [4]. Live cell imaging is an excellent method to obtain quantitative data molecular and structural events behind cell migration because of high spatial resolution with sub-second temporal resolution [5, 6]. The core purpose of all cell migration imaging studies is to correlate multiple spatiotemporal cell dynamics at the same time. The spatiotemporal dynamics include (1) structural remodeling of cell cytoskeleton (actin, tubulin), (2) movement of intracellular components (nucleus, mitochondria, endoplasmic reticulum and Golgi), (3) activating transmembrane proteins (4) surrounding mechanical and molecular cues (adhesive molecules [3, 7], external fluid stimulus [8, 9] and the extracellular matrix - ECM [10]. Cells must address these four factors that influence their migratory behavior to initiate the formation of membrane protrusions [8, 11]. The use of multiplex fluorescent labeling strategies [12] are constantly being optimized to visualize molecular and structural components of a migrating cell to identify specific molecular engines(Rho GTPases, Wasp/Scar/Wave families and ARP2/3 complex) that drives structural changes in adherent cell before it migrates. But to achieve 3D quantitative imaging with just fluorescence labeling is not trivial because of the inherent risks of photobleaching and phototoxicity [13].

Nanoscale label free imaging has emerged as an important tool to avoid photobleaching and achieve 3D quantitative imaging[14]. Nanoscale label-free imaging is achieved either by interfering scattered light with its neighboring particles in ROCS [15] or with the reflected light from a glass coverslip interface (iSCAT) [16]. Since elastic scattered light from nanoparticles and biological molecules [17] do not degrade or saturate over time [17-19], interferometric scattering has been instrumental at tracking purified proteins [18-20] and membrane protrusions [21]. However, neither ROCS nor iSCAT provide the molecular identity of molecules and cellular structures. Lately, the direct combinations of ROCS with total internal reflection fluorescence microscopy-TIRF [15] and iSCAT with fluorescence confocal[16] have begun to play an important role for nanoscopic correlative imaging. The complementary elements of fluorescence and label free nanoscale imaging permit quantitative 3D spatial temporal detail of individual cellular components that will define the next generation of nanoscopy to study cell migration.

In this paper, we demonstrate that for the first time, combined three imaging modalities (ROCS[15, 22], iSCAT[23], HiLo[24, 25]) in an oblique illumination system using a single laser source

and 2 cameras. While ROCS and HiLo are constructed on an oblique scanning system, iSCAT imaging has not been reported to use an oblique illumination system before [26]. In the following sections, we first outline the optical design (scanning angle and Fourier amplitude filter) necessary to obtain iSCAT, ROCS and HiLO in an oblique illumination imaging system. Secondly, we carried out calibration experiments to measure and compare the imaging sensitivity of iSCAT, ROCS and HiLo using 20 nm, 100 nm and 200 nm nanoparticles along axial and lateral direction [18]. We then applied the combined imaging platform we study two cell types that actively migrate in response to vessel injury. Thirdly, we establish biological goals for iSCAT, ROCS and HiLo imaging experiments to achieve. In the first imaging experiment, we examine platelets that are thought to generate filipodium protrusions that spans several platelet lengths (~ 5-10 μm) [27,28, 29] to form a biomechanical plug [30, 31]. Platelet can direct their migration to scavenge adhesive molecules bound to a stiff substrate [4], that links their role as cellular scavengers to collect molecular agents. In the second imaging experiments, we carried out imaging on endothelial cells that migrate to repair the inner lining of damaged vasculature [32]. We used fluorescence imaging to study real-time platelet migration on glass surfaces coated with fluorophore-labelled fibrinogen and crossed-linked fibrinogen- fibrin, in the presence and absence of Bovine serum albumin (BSA)- common protein in blood. Mitochondrial shape and signaling in endothelial cells are known to influence cell migration, proliferation, and tissue reorganization [33-35]. The mitochondria 3D network needs to fragment (*i.e.* by mitochondria fission) [35, 36] to smaller units that can be more readily transported across the cell [34] to provide energy for cell movement. Using fluorescence labelling of the mitochondria, we identify and measured the axial motion of mitochondria in migrating endothelial cells. We show that regions of the mitochondria between the leading edge and nucleus exhibit higher axial motion. In the two biological imaging experiments, we focused on correlating the spatial organization of membrane, organelles in subcellular regions of cells [33, 35, 37] along edge of cell membrane (leading and rear edge) [38] that orchestrates cell migration. Combined oblique imaging with interference and scattering permits us to quantify membrane fluctuations of migrating cells platelets and endothelial cells at the leading and rear edge and leverage fluorescence to identifying surface molecules or intracellular organelle that regulate cell migration.

## Results

### Oblique angle and amplitude Fourier filter to determine iSCAT and ROCS

Oblique illuminated azimuthal scanning microscope systems are frequently used in ROCS [22], HiLO [24, 25] and COSI [39] to achieve high contrast imaging for both fluorescence and scattered but not interference. ROCS[22] is not optimized for interference because the back-reflection intensities are unbalanced at HILO or TIR illumination angles. We first determined the oblique illumination angle critical to achieve interference imaging. In interference imaging (iSCAT or reflectance interference contrast-RIC) [40-43] , the interference signal is primarily optimized by balancing intensities reflected from a glass coverslip with weak scattered light from nanoparticles or biological sample using apodised optics [26, 42]. The use of azimuthal scanning in oblique illumination would, in theory, generate significantly higher background light than the weakly scattered light from samples. A dominant reflected light intensity under a HiLO or TIR angle weakens interferometric imaging sensitivity [18] and cannot be used to detect nanoparticles e.g., gold, purified protein, virus particles [40, 41, 44-46]. In an oblique scanning imaging system, we empirically observed that the signal to noise ratio (SNR) of the interference signal is directly dependent on both the oblique angle and the position of an amplitude filter placed at the Fourier plane. A balance between the intensity of reflected light from the glass slide and light scattered from the object is required to achieve the optimal imaging contrast in interferometry-based methods by modifying the incidence angle and diameter of the amplitude filter. In supplementary Figure S3, we showed that the amount of back-reflection increases exponentially at larger angles (> 40°, Supplementary Figure S3), with a shift of oblique angle from 20° to 60°. To effectively switch between interference, scattering and fluorescence microscopy, we need to simply switch between the scanning angles as shown in Figure. 1A, where we projected 3 annular scanning illumination paths (red, blue and green) implemented on a single high numerical aperture (NA) objective lens of 1.49. The interference of back-reflection and the scattered light is collected here is at an illumination angle of 20°-35° (~N.A. = 1.49), that differs from ROCS where the authors retrieved the interference signal at a much larger angle (N.A. = 1.2 and 1.46).

Supplementary Figure. S1 describes the optical design and setup in detail. During imaging, a single laser beam (wavelength, λ= 488 nm) is directed onto a two-axis galvanometer and conjugated onto the back focal plane of the objective lens. The two-axis galvanometer allows precise adjustment to different scanning radii which in turn selects the imaging mode (Scattering, Interference, and Fluorescence). While fluorescence imaging (green) can be obtained from any azimuthal scanning pattern [25, 47], interference and scattering-only images [22, 42] are separated by two scanning radii (red, blue). Experimentally, this can be determined and

preset, as shown in Fig. 1B on conjugated back focal planes (BFP). Here, interference contrast is maximized without using specialized partially reflective mirror [42]. When oblique angle θ exceeds 50°, a single diaphragm needs to be placed at the BFP of the imaging lens to balance out the reflected intensities; coverglass and particles, (Supplementary Figure. S2, S3, S4). By fixing the aperture of the diaphragm, we image in iSCAT when the illumination is less than 50° and in ROCS when the illumination angle is greater 50° (Figure S3). The iris diaphragm has zero transmittance on the edge and will not induce phase shift. We first tested the combined imaging of fixed fibroblast cells adhered on a glass coverslip. Fig. 1C (i) to (vi) shows a sequence of interference, scattering and fluorescence images of F actin (phalloidin) fibroblast cells under different oblique illumination angles from 22° to 63°. Fig. 1D and E shows the magnified view at the filopodia region and the raw intensities, measured from a set of filopodia protrusions. The detection sensitivity of the interference signal (θ = 22°) is boosted by the negative to positive contrast, as the filopodia in negative contrast can be identified compared with scattering detection. Except for the use of false colormap to represent interference signals in Fig. 1C (i), no postprocessing was performed. Fluorescence images taken at oblique illumination angles (θ = 60°, 63°) displayed increased contrast than oblique angle (θ = 22°).

Interferometric scattering signals, shown in Fig. 1C i) and D) provided a negative contrast [43, 48] because of the cosine term in the interferometric component $2E_rE_s cos\phi$[49], where $E_r$, is the reflected electric field from the coverslip, $E_s$ is scattering electric field from the sample and ϕ is the relative phase difference between $E_r$ and $E_s$. Scattering cross-section of the sample ($E_s$) will scale nonlinearly with particle size, where $E_r$ will scale with just reflecting angle. In other words, a smaller object will thereby have lower scattering ($E_s$) and Er changes with just angle. As with any interference signal, the balance of Er and Es are necessary for high fringe contrast. Because of sample variability, the visibility of the interference fringes in an interferometric scattering signal (iSCAT) require the balancing between Er and Es as shown in Fig. 2.

We next investigated detection limit of each imaging mode, interferometry, scattering and fluorescence using gold and polymer nanoparticles. Fig. 2A to D compares imaging contrasts of interference, scattering and fluorescence using signal to noise ratio (SNR) by scanning oblique angle from 5.7° to 76.8 °. Details of SNR for both negative and positive contrast is detailed under Method section. We chose a range of gold nanoparticles with mean diameter 20± 6.3 nm, 40± 8.9 nm and 60± 17 nm and fluorescence beads of 200 nm (as

specified by the manufacturer). The nanoparticle diameters were chosen because cross-section of gold scales exponentially below 100 nm, modeled in Fig. S3, which influence the scattering intensity ($I_s$). Fig. 2A and 2B shows gold nanoparticles with 20nm, 40nm and 60 nm under various oblique illumination angle. For gold nanoparticles, we only compare the interference and scattering signal in water. SNR results for 20 nm gold with a low scattering cross-section of 1.32 $nm^2$ (~1.6% of total surface area) is much higher in interference than scattering imaging. Fig. 2A show that scattered SNR (Is) nanoparticles exhibit an SNR of 0.08 ± 0.022 whereas the interference SNR ( $\frac{\mathrm{Is}.2E_rE_s\cos\phi}{\mathrm{Ir}}$) [49] is about 37% higher (0.11 ± 0.022) Conversely, we showed that an increase of the scattering cross-section by orders of magnitudes, ~ 81.3 $nm^2$ (40 nm gold nanoparticle) and 791 $nm^2$ (60 nm gold nanoparticle) results in higher scattering SNR when compared with interference SNR as shown in Fig. 2B. Fig. 2B showed that scattering SNR reached a value of 3.25 ± 0.97 to 0.566 ± 0.05 which are higher than the value of interference SNR that hovers around 0.278 ± 0.05 to 0.60 ± 0.27. Our finding shows that interference SNR ($2E_rE_s cos\phi$) [49] can play a significant role to improve imaging contrast when particles have small scattering cross-section of around 1.32 $nm^2$. Next we compare particles size with diameter of 200 nm. Fig. 2C and D compares the interference, scattering and fluorescence SNR of 200 nm polystyrene beads. Fig.2C and D compare the interference, scattering and fluorescence SNR of 200 nm polystyrene beads with a scattering cross-section of 4866 $nm^2$ that is over 3 orders of magnitude higher than observed for 20 nm gold nanoparticles. Scattering SNR in 200 nm polystyrene beads has value of 15.19 ± 1.42 that is close to 10-fold higher than interference SNR with value of 1.13 ± 0.05. To briefly summaries, the diaphragm placed at imaging BFP acts as an intensity apodizer. This meant that at oblique illumination angles from θ=10° to 40°, we achieve interferometric imaging. Beyond oblique angles of θ>50°, scattering imaging is achieved. By simply shifting the oblique illumination angle, nanoparticles of sizes from 20 nm to 200 nm can be readily imaged by interference. Azimuthal scanning removes coherent speckle noise and artifacts that are present in interferometry, scattering and fluorescence [22, 47]. In addition to the illumination angle, the polarization of illumination and sample-scattered light can also affects the interferometry signal.

Interferometric SNR would naturally possess axial information that can be used to retrieve a 3D point spread function [44]. This permits interferometric signals to track gold nanoparticle axially [41, 44] that can be developed for tracking cell membrane protrusions [50]. To calibrate this, we investigated axial interference SNR using the same nanoparticles sizes

ranging from 20 nm, 60 nm and 100 nm gold as well as 100 nm polystyrene. All the particles are fixed on a thin coverglass which is then placed on a piezo nanostage (P-736, Physik Instrument) as shown in Fig. 3A. The sample illuminated obliquely at 22$^{o}$ is swept axially through the objective focus at an interval of 10 nm step sizes. As shown in Fig. 3B and C, for 60 nm and 100 nm gold nanoparticles (higher scattering cross section of 7620 nm$^2$ and 81.3 nm$^2$), the axial interferometric intensity displays a characteristic sinusoidal intensity gradient. On the other hand, when scattering cross section is reduced by an order of magnitude to ~1.32 nm$^2$, the intensity gradient followed a parabolic curve as presented Fig. 3D. The parabolic curve in 20 nm gold nanoparticles indicate that destructive interference ($cos\phi$) [49] is responsible for high axial resolution for nanometer gold scatterers. Axial interference SNR for membrane tracking used the linear region calibrated with 100 nm polystyrene sphere that has a refractive index close to actin (~1.57) [51]. Using the calibration of the interference signal (Figure 3), we estimate the axial resolution with the equation: height difference/ΔI. The axial resolution therefore scales to the sample scattering cross section. A smaller scattering cross section yields lower axial resolution (0.3 nm for 20 nm gold beads) and higher resolution with larger scattering cross sections (0.05 nm for 100 nm gold beads). In summary, Fig. 3B to E showed that the total axial tracking distance of interference for all particle sizes ranges between 0.67 to 0.7 μm.

**Imaging of single platelet migrating at the nanoscale**

Recent live imaging studies of platelets have showed different biomechanical actions associated with platelet membrane protrusions. Platelet filopodium was observed to make "hand over hand" actions on fibrin fibers[52]. Platelet have been seen to migrate with formed lamellipodium when exposure to pathogens on coated fibrinogen surfaces. We previously demonstrated that high speed label-free platelet imaging, with rotating coherent scattering (ROCS) [22, 53] ,captured unlabeled platelet generating rodlike-extension filopodia instead of thin-sheet lamellipodia to directly attach onto single collagen fibril under arterial fluid shear [39, 54]. ROCS alone is insufficient to investigate other platelet morphodynamics along the axial direction as well as membrane surface signaling processes. We now overcome the limitation by using combined fluorescence, interference and scattering imaging to study platelet lateral and axial membrane protrusions dynamics on glass surfaces coated with fibrinogen or fibrin (cross-linked fibrinogen).

For each coated surfaces, we added either add or omitted BSA to study platelet migration. Details of sample preparation and image analysis are available in supplementary materials- Methods and sample preparation and Figure. S5. We first evaluate simultaneous scattering and interference on platelet arriving onto fibrin coated surface. Unlike traditional RIC imaging, we can capture platelet adhesion from initial contact to initial stages of spreading and adhesion on fibrin-coated glass surfaces as shown in Fig. 3F. Fig. 3F shows data of simultaneous recording of both scattering and interference over a period of 447 seconds (see Movie 1)**.** While interference signals that only occurs close to the coverslip, the scattering signal suppressed background to capture floating platelet prior to adhesion at high contrast (without postprocessing). The scattering signal is sufficiently high for automated segmentation and tracking. The interference signal is used to quantify axial displacements on those membrane protrusions as shown in Fig. 3G at 5 seconds time intervals. Fig. 3G tracks the first instances of filopodia formation during adhesion before a lamellipodium is formed (see Movie 2). To visualized migrating tracks with and without BSA, we labelled fibrinogen and fibrin with fluorescence label (Alexa Fluor 488) using previous published protocol [4, 55]. Here, migrating tracks are shown by a lost in fluorescence due to uptake of fibrin or fibrinogen coating on glass surfaces. The tracks are imaged using fluorescence imaging.

Fig. 4A(i) to (iv) shows that interference, scattering and fluorescence, using BSA treated sample (see Movie 3). Adherent platelets are seen to internalized fibrinogen and fibrin. A bright fluorescence spot can be seen located intracellularly in the platelet using fluorescence. Using scattering and interference, platelets' cellular morphology in 3D can be quantified using standard cell segmentation and profiling tools in open source program *Cellprofiler* [56]. We sorted the imaged platelets ($n_{fibrin}$=427 and $n_{fibrinogen}$ 510) against two different classifiers namely area ($\mu m^2$) and solidarity. Area is meant to show cell spreading. For platelets with a larger spread could indicating flat membrane protrusion resembling lamellipodium. Solidarity is defined by irregularity along the cell boundaries. Platelets with highly number of filopodium protrusion (finger-like) would score low on the solidarity point. Additional information on cell segmentation and morphological profiling is detailed in Fig. S5. Fig. 4 B (i) show the classifiers (area and solidarity) and the percentage of migrating platelets on fibrin and fibrinogen coated surfaces. The results showed that without the inclusion of BSA, no migration is observed (no visible tracked due to loss of fluorescence). Overall, Fig. 4B (i) showed that there are around 4 folds more platelets migrating under fibrin coated. Conversely, platelets would generally migrate on fibrinogen coated surfaces. Using the classifiers, we can further

separate the morphological profiles of the migrating and non-migrating platelets as shown in Fig. 4 B ii) and iii). Platelets on fibrin coated surface showed comparatively smaller surface area than fibrinogen coated surfaces. On the other hand, on the solidity scoring, there is no significant variation amongst the platelets either migrating or non-migrating. Overall, this meant that the platelet adhesion under spreading conditions would generate highly heterogenous morphology profiles. Such heterogenous membrane protrusion differs from our previous observation of platelet under flow on collagen matrix where scattering imaging only displayed filopodia formation and could have important implication of thrombus-based fibrinolysis. With scattering and interference signal, we carried out automated axial tracking of lamellipodium of a migrating platelet on fibrin coated surface as shown in Fig. 4C (i) (Movie 4, 5) that indicated a fluctuation from peak to peak height displacement of around 0.13 µm as shown in Fig. 4C (ii). In Fig. 4C (iii), we then compared both the leading and rear edge of the migrating platelet by plotting the overall axial fluctuations. The leading edge showed a normal distribution of membrane displacement centered at 0 (*i.e.* no protrusion or retraction). However, the leading edge exhibited membrane fluctuations of -0.13 µm (retraction) to 0.13 µm (extension), shown as two peaks in Figure 4C, iii). Out of phase fluctuations indicate asynchronous behavior of cell migration inferring differences in adhesion strength [57] between the leading and rear edge.

**Imaging of Nanoscale dynamics of Mitochondria in migrating cells**

The mitochondria form a 1 micron-thick tubular network and trafficked along the cytoskeleton to distribute energy production for cell motility [33, 58]. Visualizing this mitochondrial organization in real-time relies on fluorescence labelling, which is prone to photobleaching and does not resolve the seconds-timescale remodeling of the mitochondrial 3D network necessary for cell migration [59]. Mitochondria motion is therefore challenged by the 3D space they are in: thicker cell space near the nucleus, but interlinked with the endoplasmic reticulum network [58] or thinner cell space at the leading edge (*i.e.* lamellipodia) of a migrating cell. Considering scattering and interference imaging provides both lateral and axial (Figure 3) nanometer imaging resolution, we explored whether both imaging modalities resolve mitochondria 3D structure and displacement in migrating cells. For this, we employed microvascular endothelial cell line labelled with Mitotracker Green plated on glass-bottom culture dishes, which are commonly studied in scratch wound assays to investigate migration during vascular injury [32]. Our initial results found significant photobleaching of Mitotracker fluorescence resulting in 30% of fluorescence intensity over 3 minutes (Supplementary Figure.

S6). To overcome this, we synchronized the laser emission to the scanning frequency to generate a pulse of 0, 2, 10 or 20 Hz (Figure 5A and supplementary methods). We found that increasing the laser pulse rate to 2 Hz reduced photobleaching by 15% and maximum reduction of photobleaching by 25% with 10 and 20 Hz pulse (Supplementary Figure. S6). Hence, to minimize photobleaching and phototoxicity we conducted all mitochondria imaging experiments with 20 Hz laser pulsing.

Under scattering and interference imaging, we observed tubular structures extending 25 µm outward from the perinuclear region (Figure 5A (ii)). These structures split and converged along its length, consistent with a mitochondrial network under persistent fusion and fission. Interference imaging revealed fringe shifts that were unique to the tubular structures and not the entire cell. To confirm these were mitochondrial networks, we stained HMVEC cells with a mitochondria-specific fluorescent dye, Mitotracker Green (Figure 5A (ii)), which confirmed the observed tubular structures were mitochondria. Figure 5B (i) and (iv) shows that the Mitotracker fluorescence signal is used as a mask to segment mitochondria in the interference (Figure 5B (ii)) or scattering image (Figure 5B (v)). Figure 5B (iii) shows a relative axial position map of individual mitochondria filaments retrieved calibrating the fringe shift to axial distance in Figure 3. The scattering image complements the axial information, providing the lateral position of the mitochondria (Figure 5B (vi)).

Our quantitation of mitochondria relative axial position reveals a morphology with multiple bends across its length. We next measured the variation of mitochondria axial movement across a migrating cell (Figure 5C and see Movie 6). Figure 5C (i) shows the axial shifts across a mitochondrion of 45 µm length taken 20 seconds apart. We observed axial shifts of up to 350 nm within a length of 2 µm and regions of increased axial motion that was centered in the middle (~20 µm) of the mitochondrion. Interference imaging also revealed the mitochondrion stretched up to 15 µm away from the leading edge of the cell, where the cell actively formed membrane protrusions and expanded its boundary by 3.8 µm (see Movie 6). Having found a variance in mitochondria axial motion, we examined if proximity to the cell's boundary affected mitochondrial motion. Preliminary evidence suggests that mitochondria bind to focal adhesions [60], which may constrict mitochondria motion. Figure 5C (ii) shows the axial displacement of the mitochondria in Figure 5C (i), measured between 22 – 38 µm distance from the leading edge of the cell. Mitochondria axial motion ranged between 10 nm/s to 100 nm/s and was maximal at 28 µm away from the cell boundary. These results support our observation from Figure 5C (i). We suggest that mitochondria tethered to the endoplasmic

reticulum network and focal adhesions may play a role in regulating mitochondria motility [33, 34]. Through combined interference and fluorescence imaging of the mitochondria and cell membrane, we additionally visualized the distribution of mitochondria centered around the nucleus of the cell and its entry into the nucleus (Video 7).

## Conclusion

Nanoscale live cell imaging illuminates our fundamental understanding of cell migration. Existing nanoscopic imaging tools are broadly classified into separate fluorescence [14], scattering [22, 53] and interferometry platforms.[18, 19]. We demonstrated a direct means to combine scattering, interferometry and fluorescence imaging modalities system using a single laser source with azimuthal laser scanning and dual digital cameras. Most importantly, we identified that a Fourier amplitude filter is necessary to perform interferometric imaging [47] using azimuthal scanning that is able to balance intensities reflected from a glass coverslip with weak scattered light from nanoparticles or biological sample without using apodised optics [26, 42]. In ROCS, the aperture of the diaphragm needs to be changed when switching imaging mode whereas the aperture of the diaphragm here is fixed. Hence, in the combined imaging platform can switch between interference and scattering imaging modes for simultaneous multimodal imaging. In the current combined imaging system, we do not use background subtraction that is used in ROCS and iSCAT. We are able to obtain high contrast imaging (sensitivity up to 20 nm gold nanoparticle) that does not need background removal in real time. The combined oblique illumination modality unifies iSCAT, ROCS and HiLO into a single unit and has shown to be applicable for a multitude of imaging experiment that investigate spatial organization of intracellular organelles [61], ligand or lipid coating on substrates surfaces [62] that are necessary for cells to migrate [33]. iSCAT possess an axial resolution of lower than 100 nm whereas in ROCS or HiLO, the axial resolution is chiefly determined by the thickness of the inclined plane.

The next step is to apply the combined imaging platform to study membrane receptor clustering [63], intracellular calcium flux [64], actin polymerization [65] while continuous tracking morphological changes in cell migration assays. We further anticipate that the combined imaging can possibly resolve nanoscale membrane curvatures [66], membrane pores[67], transmembrane proteins and receptors,[68, 69] as well as external mechanical forces[70] that influence the formation of membrane protrusions (lamellipodia, ruffles, filopodia). While we have shown that the combined imaging technical can be applicable to both anucleate and nucleated cells, the limitation of iSCAT when combined is the limited imaging depth of ~ 0.7

μm. Finally, the current iSCAT imaging do not use any form of post-processing and we postulate that detection sensitivity could be further enhanced by using ratiometric subtraction.

**Acknowledgement**

We thank Ms. Sarah Hicks and Mr. Junxiang Zhang for providing washed platelets and fibroblast samples. Funded Australian Research Council (DE160100843, DP190100039, DP200100364) and NHMRC (IDEAS)

**Contribution**

W.M.L. conceived and supervised the project. Y.Z. built the imaging system and performed all platelet experiments. Y.J. L develop live cell imaging chamber and conducted intracellular imaging on endothelial cells, H. L developed the automated image tracking method, T Xu advice on optical design, Y.L.T. prepared washed platelet samples, E.E.G advised on platelet experiments, V D-A and C Parish advised on endothelial cell experiments, and. Y.Z. carried out the data analysis along with H.L (*Intensity tracking*) and C.L. (*Cell profiler*). Y. Z, Y.J.L and W.M.L. wrote the manuscript with input from all authors.

**Figure.1 – Combined Interference, Scattering and Fluorescence Imaging**

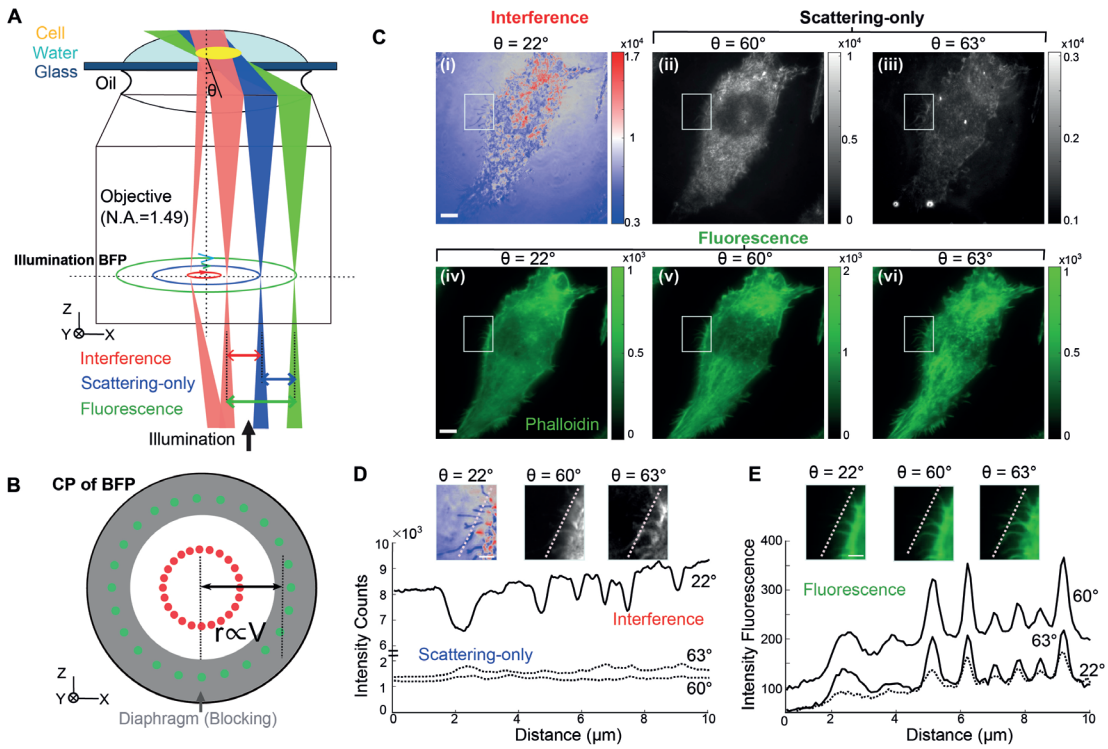


**Figure 1** (**A**) An oblique beam (with angle θ corresponding to optical axis) is radically scanning at back focal plane (BFP) of the 1.49 NA objective. When θ = 10° to 40° (red), the interference of back-reflection from the coverslip and scattered light will be collected by the detector, and when θ > 50° (green), the back-reflection will be blocked by a diaphragm at conjugation plane (CP) of BFP that only allow pure scattering to be detected (darkfield). The fluorescence signal (blue) will be collected simultaneously at corresponding angles without blocking due to the dual camera detection scheme. (**B**) The position of the scanning pattern and the diaphragm at CP of BFP, where the gray area, red and green pattern represent region of diaphragm, scanning pattern of interference and pure scattering detection respectively. (**C**) Interference, scattering and fluorescence images of fixed fibroblast (labelled with Alexa Fluor 488 conjugated Phalloidin) at three different angles: 22°, 60° (Hilo) and 63° (TIRF). Scale bar = 5 μm. Zoomed view at the filopodia region (**D**) for scattering and interference, and (**E**) for fluorescence detection at the indicated angle. The intensity profile along the filopodia region as indicated in inlet images (white dotted line) are plotted accordingly. Scale bar = 2 μm.

**Figure 2 – Azimuthal illumination angle controls Interference, Scattering and Fluorescence Signal**

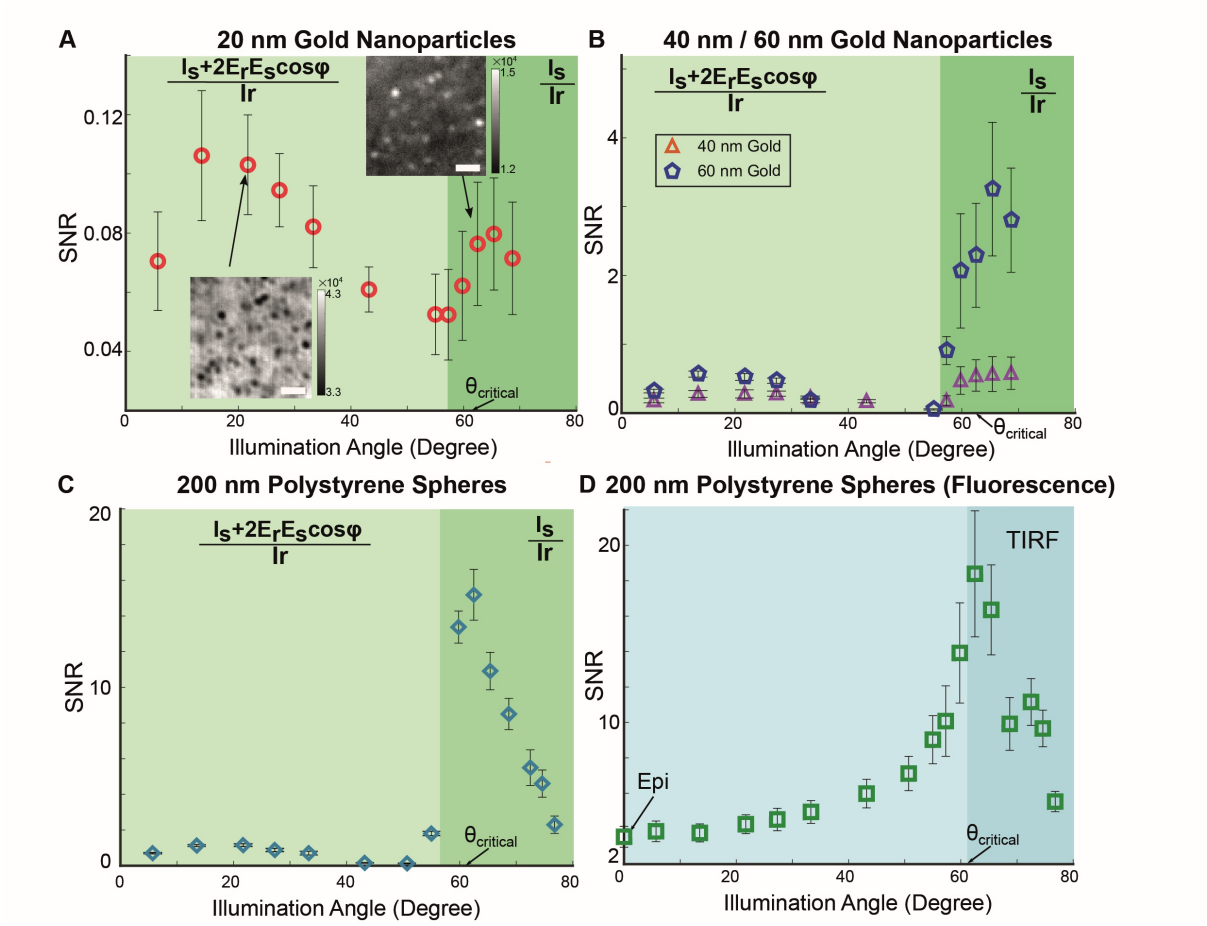


Figure 2 **Quantification of signal to noise ratio of nanoparticles ranging from 20 – 200nm (diameter) with scattering and fluorescence detection.** SNR of (A) 20 nm, (B) 40 nm and 60 nm gold nanoparticles and (C) 200 nm polystyrene using scattering detection under different illumination angle ranging from 5° to 70°, where diaphragm is set to block back-reflection at 57° and the critical angle is at 63°. Inlet images in (A) are interference and pure scattering signal of the particles at 22° and 63° respectively. Scale bar = 1 µm. (D) SNR of the 200 nm polystyrene with fluorescence detection, where the critical angle is at 63°. Error bar = standard derivation from measurement of at least 50 nanoparticles.

1 **Figure 3 – Axial SNR of interference fringes**

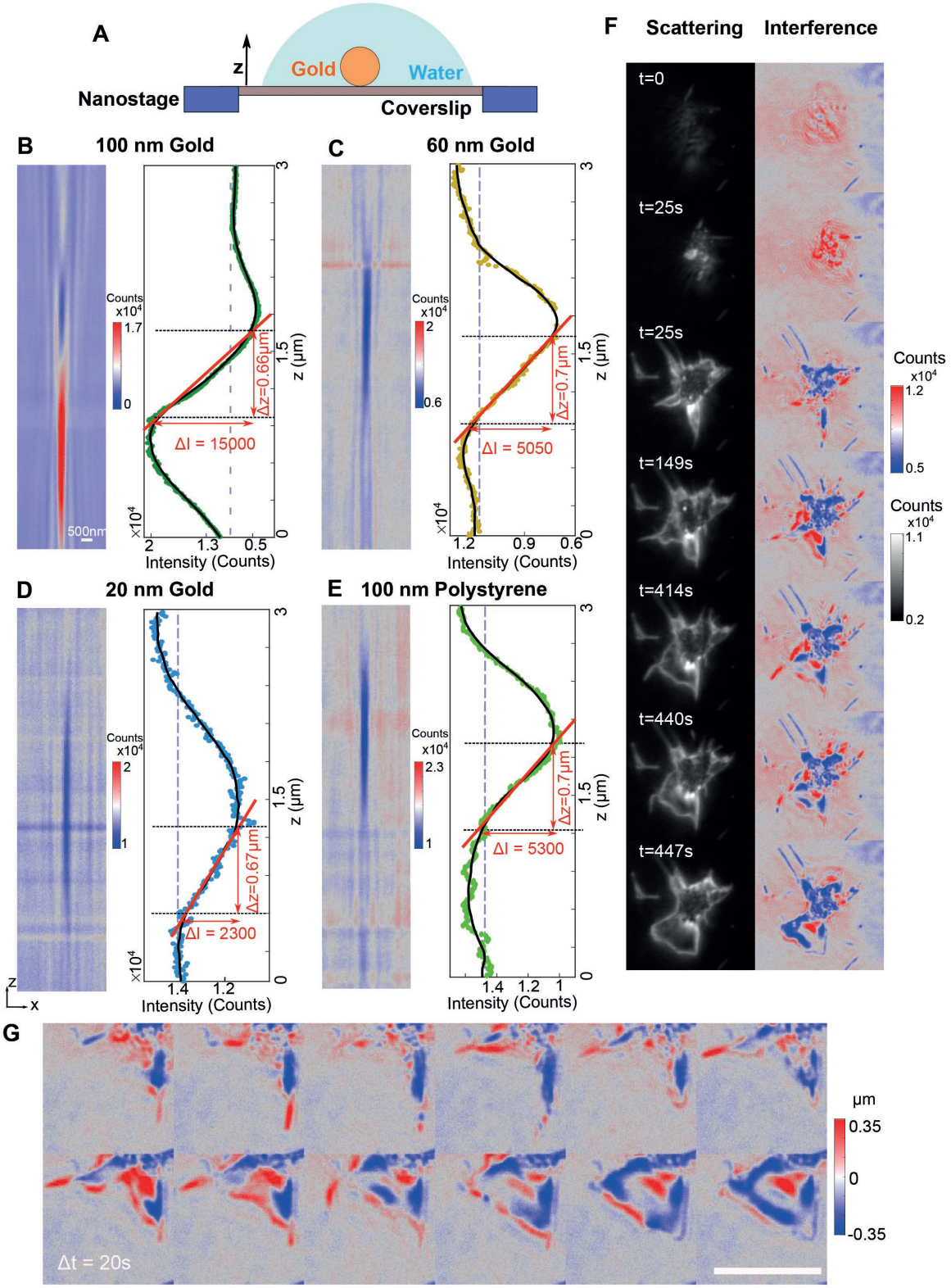


2

Figure 3 **Calibrating axial intensity profile and displacement with nanoparticles from 20 nm to 100 nm**. (A) To record the intensity profile of gold/polystyrene nanoparticles, we firstly dried the particles on a coverslip and then immersed with water. The coverslip was place on a piezo nanostage that allows axial sweeping of the sample across the focus at 10 nm steps. The axial intensity map along with the line profile of gold nanoparticles at (B) 100 nm, (C) 60nm and (D) 20nm, and (E) polystyrene nanoparticles at 100 nm are plotted as scattered plot, the black line indicates the moving average of 30 points. The red line represents the relation between intensity ($\Delta I$) and axial displacement ($\Delta z$). (F) Simultaneous recording of both scattering and interference over a period of 447 seconds showing early platelet adhesion, filopodia and lamellipodia formation and spreading on fibrin surfaces. (Movie 1) Scale bar = 5 µm. (G) Axial displacements of the membrane protrusions at 20 seconds time intervals. (Movie 2)

1 **Figure 4 – Quantifying platelet migration**

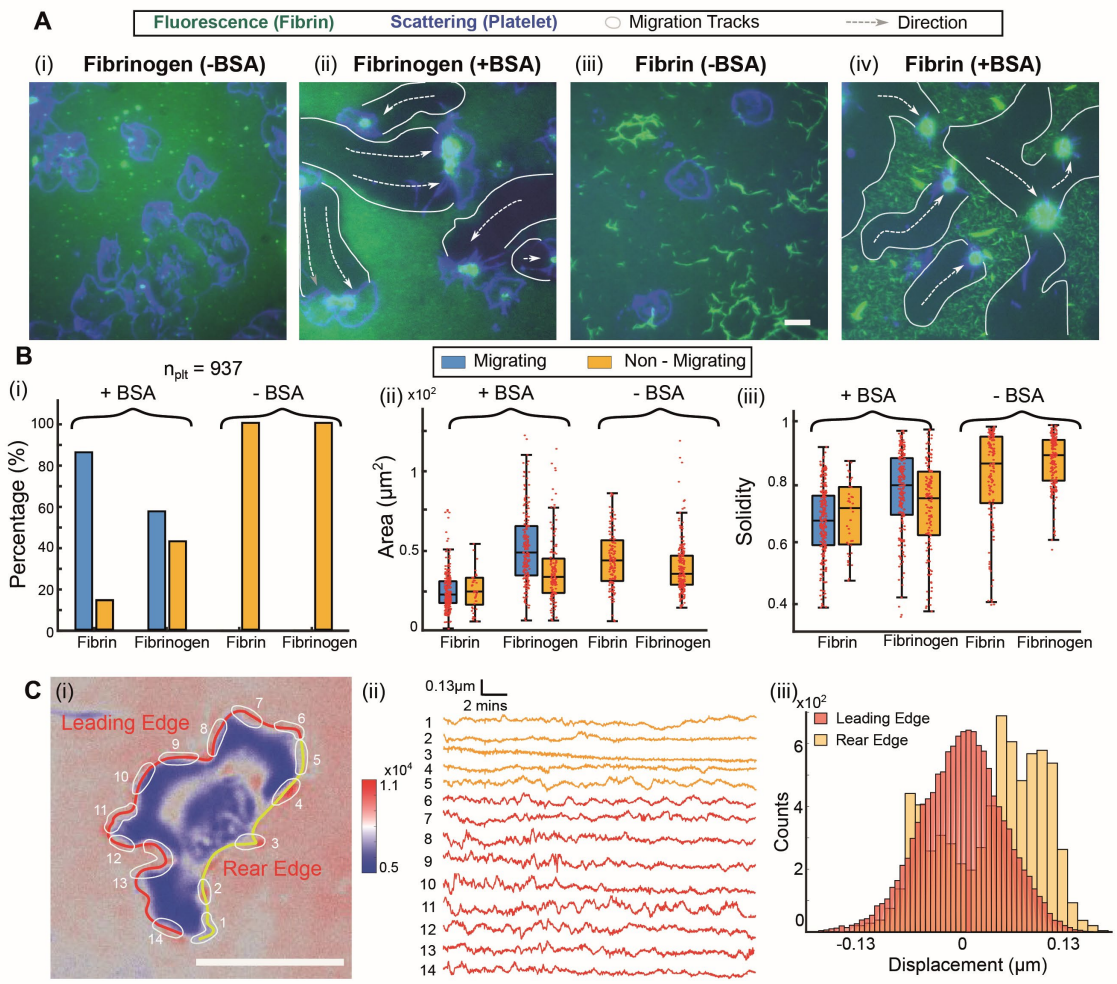


2

3 Figure 4 **Tracking platelet migration on fibrin/fibrinogen coated surface.** (A) Combined
4 fluorescence and scattering signal of single platelet migration on fibrin (Movie 3) and
5 fibrinogen coated surfaces with/without BSA. Green channel and blue channel are fluorescence
6 and scattering signal respectively. The trajectory of platelet movement is highlighted with
7 white broader with white arrow indicating predicted direction of migration. (B) Quantification
8 of platelet migration and morphology (area and solidity) with four types of coating. Platelet
9 morphology is quantified through cell profiler. Number of platelets quantified: n = 427 and n
10 = 510 for fibrin and fibrinogen coated surface respectively. (C) (i) Interference signal of a
11 migrating platelet on fibrin coated surface. (ii) The axial displacement along the leading edge
12 and rear edge is tracked during 25 minutes of spreading, with orange and red represent rear and
13 leading edge respectively (Movie 4, 5). (iii) Histogram showing the counts on axial
14 displacement of rear and leading edge.

15

**Figure 5- Live cell quantitation of mitochondria distribution**

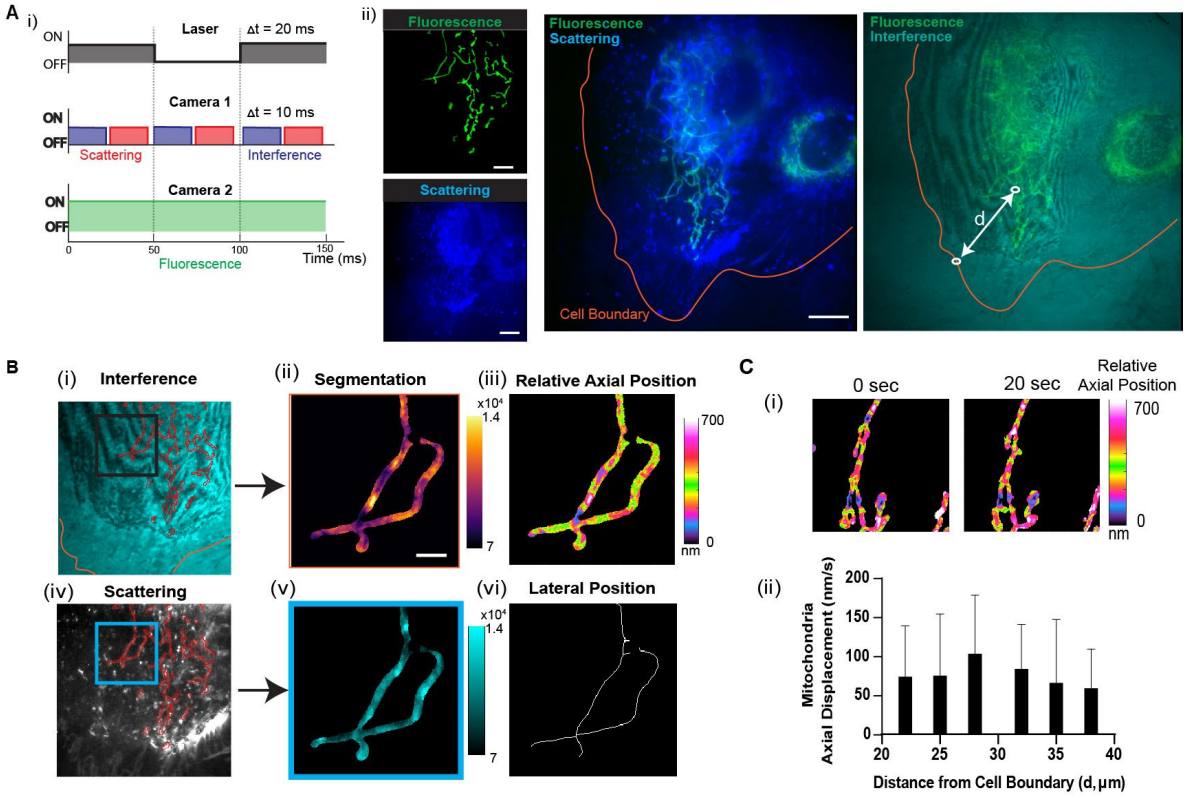


Figure 5. **Tracking of mitochondria axial position in endothelial cells. (A, i)** Diagram showing laser pulse synchronized to camera 1 (scattering and interference imaging) and camera 2 (fluorescence imaging) to reduce photobleaching. (ii) The fluorescence, scattering and interference images of HMVEC cell labelling of mitochondria with Mitotracker Green. (B) The mitotracker fluorescence signal for (ii, v) masking and segmenting mitochondria in the (i-iii) interference and (iv-vii) scattering images. (iii) The interference intensity is converted to relative axial position using the calibrated axial intensity profile from Figure 3 and (vi) scattering image provides lateral position of the mitochondria. (C, i) The relative axial position of mitochondria in HMVEC cells retrieved from interferometry and (ii) plot of axial mitochondria displacement as a function of distance from the cell's leading edge. Data are S.D. of n=9 data points.

## References


1 Dustin, M. L. The Immunological Synapse. *Cancer Immunology Research* **2**, 1023-1033, doi:10.1158/2326-6066.Cir-14-0161 (2014).

2 Guerrero-Juarez, C. F. *et al.* Single-cell analysis reveals fibroblast heterogeneity and myeloid-derived adipocyte progenitors in murine skin wounds. *Nature Communications* **10**, 650, doi:10.1038/s41467-018-08247-x (2019).

3 Mattila, P. K. & Lappalainen, P. Filopodia: molecular architecture and cellular functions. *Nature Reviews Molecular Cell Biology* **9**, 446-454, doi:10.1038/nrm2406 (2008).

4 Gaertner, F. *et al.* Migrating Platelets Are Mechano-scavengers that Collect and Bundle Bacteria. *Cell* **171**, 1368-1382.e1323, doi:10.1016/j.cell.2017.11.001 (2017).

5 Dormann, D. & Weijer, C. J. Imaging of cell migration. *The EMBO Journal* **25**, 3480-3493, doi:https://doi.org/10.1038/sj.emboj.7601227 (2006).

6 Wöllert, T. & Langford, G. M. in *Cytoskeleton Methods and Protocols* (ed Ray H. Gavin) 3-21 (Humana Press, 2010).

7 Yeoman, B. *et al.* Adhesion strength and contractility enable metastatic cells to become adurotactic. *Cell Reports* **34**, 108816, doi:https://doi.org/10.1016/j.celrep.2021.108816 (2021).

8 Yamada, K. M. & Sixt, M. Mechanisms of 3D cell migration. *Nature Reviews Molecular Cell Biology* **20**, 738-752, doi:10.1038/s41580-019-0172-9 (2019).

9 Lee, H. J. *et al.* Fluid shear stress activates YAP1 to promote cancer cell motility. *Nature Communications* **8**, 14122, doi:10.1038/ncomms14122 (2017).

10 Fassett, J., Tobolt, D. & Hansen, L. K. Type I Collagen Structure Regulates Cell Morphology and EGF Signaling in Primary Rat Hepatocytes through cAMP-dependent Protein Kinase A. *Molecular Biology of the Cell* **17**, 345-356, doi:10.1091/mbc.e05-09-0871 (2006).

11 Gaertner, F. *et al.* WASp triggers mechanosensitive actin patches to facilitate immune cell migration in dense tissues. *Developmental Cell* **57**, 47-62.e49, doi:https://doi.org/10.1016/j.devcel.2021.11.024 (2022).

12 Dean, K. M. & Palmer, A. E. Advances in fluorescence labeling strategies for dynamic cellular imaging. *Nature Chemical Biology* **10**, 512-523, doi:10.1038/nchembio.1556 (2014).

13 Hoebe, R. A. *et al.* Controlled light-exposure microscopy reduces photobleaching and phototoxicity in fluorescence live-cell imaging. *Nature Biotechnology* **25**, 249-253, doi:10.1038/nbt1278 (2007).

14 Schermelleh, L. *et al.* Super-resolution microscopy demystified. *Nature Cell Biology* **21**, 72-84, doi:10.1038/s41556-018-0251-8 (2019).

15 Jünger, F. *et al.* 100 Hz ROCS microscopy correlated with fluorescence reveals cellular dynamics on different spatiotemporal scales. *Nature Communications* **13**, 1758, doi:10.1038/s41467-022-29091-0 (2022).

16 Hsiao, Y.-T., Tsai, C.-N., Cheng, C.-Y. & Hsieh, C.-L. Molecularly Specific and Functional Live Cell Imaging by Label-Free Interference Microscopy. *ACS Photonics* **9**, 2237-2245, doi:10.1021/acsphotonics.2c00599 (2022).

17 Boyer, D., Tamarat, P., Maali, A., Lounis, B. & Orrit, M. Photothermal Imaging of Nanometer-Sized Metal Particles Among Scatterers. *Science* **297**, 1160-1163, doi:doi:10.1126/science.1073765 (2002).

18 Young, G. & Kukura, P. Interferometric Scattering Microscopy. *Annual Review of Physical Chemistry* **70**, 301-322, doi:10.1146/annurev-physchem-050317-021247 (2019).

19 Cotte, Y. *et al.* Marker-free phase nanoscopy. *Nature Photonics* **7**, 113-117, doi:10.1038/nphoton.2012.329 (2013).

20 Piliarik, M. & Sandoghdar, V. Direct optical sensing of single unlabelled proteins and super-resolution imaging of their binding sites. *Nature Communications* **5**, 4495, doi:10.1038/ncomms5495 (2014).

21 Taylor, R. W. *et al.* Interferometric scattering microscopy reveals microsecond nanoscopic protein motion on a live cell membrane. *Nature Photonics* **13**, 480-487, doi:10.1038/s41566-019-0414-6 (2019).

22 Ruh, D., Mutschler, J., Michelbach, M. & Rohrbach, A. Superior contrast and resolution by image formation in rotating coherent scattering (ROCS) microscopy. *Optica* **5**, 1371-1381, doi:10.1364/OPTICA.5.001371 (2018).

23 Dejardin, M.-J. *et al.* Lamellipod Reconstruction by Three-Dimensional Reflection Interference Contrast Nanoscopy (3D-RICN). *Nano Letters* **18**, 6544-6550, doi:10.1021/acs.nanolett.8b03134 (2018).

24 Guo, Y. *et al.* Visualizing Intracellular Organelle and Cytoskeletal Interactions at Nanoscale Resolution on Millisecond Timescales. *Cell* **175**, 1430-1442 e1417, doi:10.1016/j.cell.2018.09.057 (2018).

25 Tokunaga, M., Imamoto, N. & Sakata-Sogawa, K. Highly inclined thin illumination enables clear single-molecule imaging in cells. *Nature Methods* **5**, 159-161, doi:10.1038/nmeth1171 (2008).

26 Dominika, J., Kristyna, H., Milan, V. & Marek, P. in *Proc.SPIE.*

27 Pleines, I. *et al.* Multiple alterations of platelet functions dominated by increased secretion in mice lacking Cdc42 in platelets. *Blood* **115**, 3364-3373, doi:https://doi.org/10.1182/blood-2009-09-242271 (2010).

28 Pierre, H. M. *et al.* Immobilized fibrinogen activates human platelets through glycoprotein VI. *Haematologica* **103**, 898-907, doi:10.3324/haematol.2017.182972 (2018).

29 Montague, S. J. *et al.* Fibrin exposure triggers αIIbβ3-independent platelet aggregate formation, ADAM10 activity and glycoprotein VI shedding in a charge-dependent manner. *Journal of Thrombosis and Haemostasis* **18**, 1447-1458, doi:https://doi.org/10.1111/jth.14797 (2020).

30 Kaneva, V. N. *et al.* Modeling Thrombus Shell: Linking Adhesion Receptor Properties and Macroscopic Dynamics. *Biophys J* **120**, 334-351, doi:10.1016/j.bpj.2020.10.049 (2021).

31 Sandmann, R. & Koster, S. Topographic Cues Reveal Two Distinct Spreading Mechanisms in Blood Platelets. *Sci Rep* **6**, 22357, doi:10.1038/srep22357 (2016).

32 Liang, C. C., Park, A. Y. & Guan, J. L. In vitro scratch assay: a convenient and inexpensive method for analysis of cell migration in vitro. *Nat Protoc* **2**, 329-333, doi:10.1038/nprot.2007.30 (2007).

33 Cunniff, B., McKenzie, A. J., Heintz, N. H. & Howe, A. K. AMPK activity regulates trafficking of mitochondria to the leading edge during cell migration and matrix invasion. *Mol Biol Cell* **27**, 2662-2674, doi:10.1091/mbc.E16-05-0286 (2016).

34 Zhao, J. *et al.* Mitochondrial dynamics regulates migration and invasion of breast cancer cells. *Oncogene* **32**, 4814-4824, doi:10.1038/onc.2012.494 (2013).

35 Lopez-Domenech, G. *et al.* Miro proteins coordinate microtubule- and actin-dependent mitochondrial transport and distribution. *EMBO J* **37**, 321-336, doi:10.15252/embj.201696380 (2018).

36 Madan, S., Uttekar, B., Chowdhary, S. & Rikhy, R. Mitochondria Lead the Way: Mitochondrial Dynamics and Function in Cellular Movements in Development and Disease. *Front Cell Dev Biol* **9**, 781933, doi:10.3389/fcell.2021.781933 (2021).

37 Campello, S. *et al.* Orchestration of lymphocyte chemotaxis by mitochondrial dynamics. *J Exp Med* **203**, 2879-2886, doi:10.1084/jem.20061877 (2006).

38 Ridley, Anne J. Life at the Leading Edge. *Cell* **145**, 1012-1022, doi:10.1016/j.cell.2011.06.010 (2011).

39 Zheng, Y. *et al.* Label-free multimodal quantitative imaging flow assay for intrathrombus formation in vitro. *Biophysical Journal* **120**, 791-804, doi:https://doi.org/10.1016/j.bpj.2021.01.015 (2021).

40 Taylor, R. W. & Sandoghdar, V. Interferometric Scattering Microscopy: Seeing Single Nanoparticles and Molecules via Rayleigh Scattering. *Nano Letters* **19**, 4827-4835, doi:10.1021/acs.nanolett.9b01822 (2019).

41 Gholami Mahmoodabadi, R. *et al.* Point spread function in interferometric scattering microscopy (iSCAT). Part I: aberrations in defocusing and axial localization. *Opt. Express* **28**, 25969-25988, doi:10.1364/OE.401374 (2020).

42 Cole, D., Young, G., Weigel, A., Sebesta, A. & Kukura, P. Label-Free Single-Molecule Imaging with Numerical-Aperture-Shaped Interferometric Scattering Microscopy. *ACS Photonics* **4**, 211-216, doi:10.1021/acsphotonics.6b00912 (2017).

43 Young, G. *et al.* Quantitative mass imaging of single biological macromolecules. *Science* **360**, 423-427, doi:10.1126/science.aar5839 (2018).

44 Dong, J., Maestre, D., Conrad-Billroth, C. & Juffmann, T. Fundamental bounds on the precision of iSCAT, COBRI and dark-field microscopy for 3D localization and mass photometry. *Journal of Physics D: Applied Physics* **54**, 394002, doi:10.1088/1361-6463/ac0f22 (2021).

45 Küppers, M., Albrecht, D., Kashkanova, A., Lühr, J. & Sandoghdar, V. in *Biophotonics Congress 2021.* (eds C. Maitland K. Hendon C. Wojtkowski M. Quinn K. Schanne-Klein M. Durr N. Elson D. Cichos F. Oddershede L. Emiliani V. Maragò O. Nic Chormaic S. Pégard N. Gibbs S. Vinogradov S. Niedre M. Samkoe K. Devor A. Peterka D. Blinder P. Boudoux & E. Buckley) NTh2C.5 (Optical Society of America).

46 Ortega Arroyo, J., Cole, D. & Kukura, P. Interferometric scattering microscopy and its combination with single-molecule fluorescence imaging. *Nature Protocols* **11**, 617-633, doi:10.1038/nprot.2016.022 (2016).

47 Axelrod, D. Total internal reflection fluorescence microscopy in cell biology. *Traffic* **2**, 764-774, doi:10.1034/j.1600-0854.2001.21104.x (2001).

48 Park, J.-S. *et al.* Label-free and live cell imaging by interferometric scattering microscopy. *Chemical Science* **9**, 2690-2697, doi:10.1039/C7SC04733A (2018).

49 Taylor, R. W. & Sandoghdar, V. in *Label-Free Super-Resolution Microscopy* (ed Vasily Astratov) 25-65 (Springer International Publishing, 2019).

50 Park, J.-S. *et al.* Fluorescence-Combined Interferometric Scattering Imaging Reveals Nanoscale Dynamic Events of Single Nascent Adhesions in Living Cells. *The Journal of Physical Chemistry Letters* **11**, 10233-10241, doi:10.1021/acs.jpclett.0c02103 (2020).

51 Bon, P., Lécart, S., Fort, E. & Lévêque-Fort, S. Fast Label-Free Cytoskeletal Network Imaging in Living Mammalian Cells. *Biophysical Journal* **106**, 1588-1595, doi:10.1016/j.bpj.2014.02.023 (2014).

52 Kim, O. V., Litvinov, R. I., Alber, M. S. & Weisel, J. W. Quantitative structural mechanobiology of platelet-driven blood clot contraction. *Nature Communications* **8**, 1274, doi:10.1038/s41467-017-00885-x (2017).

53 Zhang, P. *et al.* Plasmonic scattering imaging of single proteins and binding kinetics. *Nature Methods* **17**, 1010-1017, doi:10.1038/s41592-020-0947-0 (2020).

54 Schurr, Y. *et al.* Platelet lamellipodium formation is not required for thrombus formation and stability. *Blood* **134**, 2318-2329, doi:10.1182/blood.2019002105 (2019).

55 Nicolai, L. *et al.* Vascular surveillance by haptotactic blood platelets in inflammation and infection. *Nature Communications* **11**, 5778, doi:10.1038/s41467-020-19515-0 (2020).

56 Jones, T. R. *et al.* Scoring diverse cellular morphologies in image-based screens with iterative feedback and machine learning. *Proceedings of the National Academy of Sciences* **106**, 1826-1831, doi:10.1073/pnas.0808843106 (2009).

57 Barnhart, E., Lee, K.-C., Allen, G. M., Theriot, J. A. & Mogilner, A. Balance between cell−substrate adhesion and myosin contraction determines the frequency of motility initiation in fish keratocytes. *Proceedings of the National Academy of Sciences* **112**, 5045-5050, doi:10.1073/pnas.1417257112 (2015).

58 Abrisch, R. G., Gumbin, S. C., Wisniewski, B. T., Lackner, L. L. & Voeltz, G. K. Fission and fusion machineries converge at ER contact sites to regulate mitochondrial morphology. *J Cell Biol* **219**, doi:10.1083/jcb.201911122 (2020).

59 Valm, A. M. *et al.* Applying systems-level spectral imaging and analysis to reveal the organelle interactome. *Nature* **546**, 162-167, doi:10.1038/nature22369 (2017).

60 Daniel, R., Mengeta, A., Bilodeau, P. & Lee, J. M. Mitochondria tether to Focal Adhesions during cell migration and regulate their size. *bioRxiv*, 827998, doi:10.1101/827998 (2019).

61 Guo, Y. *et al.* Visualizing Intracellular Organelle and Cytoskeletal Interactions at Nanoscale Resolution on Millisecond Timescales. *Cell* **175**, 1430-1442.e1417, doi:10.1016/j.cell.2018.09.057 (2018).

62 Axelrod, D. in *Methods in Cell Biology* Vol. 30 (eds D. Lansing Taylor & Yu-Li Wang) 245-270 (Academic Press, 1989).

63 Eckert, A. F. *et al.* Measuring ligand-cell surface receptor affinities with axial line-scanning fluorescence correlation spectroscopy. *eLife* **9**, e55286, doi:10.7554/eLife.55286 (2020).

64 Jiang, Y. *et al.* An Ultrasensitive Calcium Reporter System via CRISPR-Cas9-Mediated Genome Editing in Human Pluripotent Stem Cells. *iScience* **9**, 27-35, doi:https://doi.org/10.1016/j.isci.2018.10.007 (2018).

65 Kraning-Rush, C. M., Carey, S. P., Califano, J. P., Smith, B. N. & Reinhart-King, C. A. The role of the cytoskeleton in cellular force generation in 2D and 3D environments. *Physical Biology* **8**, 015009, doi:10.1088/1478-3975/8/1/015009 (2011).

66 Groves, J. T., Parthasarathy, R. & Forstner, M. B. Fluorescence Imaging of Membrane Dynamics. *Annual Review of Biomedical Engineering* **10**, 311-338, doi:10.1146/annurev.bioeng.10.061807.160431 (2008).

67 Shin, W. *et al.* Visualization of Membrane Pore in Live Cells Reveals a Dynamic-Pore Theory Governing Fusion and Endocytosis. *Cell* **173**, 934-945.e912, doi:https://doi.org/10.1016/j.cell.2018.02.062 (2018).

68 Kanchanawong, P. *et al.* Nanoscale architecture of integrin-based cell adhesions. *Nature* **468**, 580-584, doi:10.1038/nature09621 (2010).

69 Poulter, N. S. *et al.* Platelet actin nodules are podosome-like structures dependent on Wiskott–Aldrich syndrome protein and ARP2/3 complex. *Nature Communications* **6**, 7254, doi:10.1038/ncomms8254 (2015).

70 Oakes, P. W. *et al.* Lamellipodium is a myosin-independent mechanosensor. *Proceedings of the National Academy of Sciences* **115**, 2646-2651, doi:10.1073/pnas.1715869115 (2018).

**Supplementary Files**

# Combined Scattering, Interferometry and Fluorescence oblique illumination for live cell nanoscale imaging

**Yujie Zheng [1,2,⸸], Yean Jin Lim [1,2,⸸], Hanqi Lin[1,2], Tienan Xu[1,2], Carmen Longbottom [1,2], Viviane Delghingharo-Augusto[1], Yee Lin Thong [1], Christopher Parish[1], Elizabeth E Gardiner[1], Woei Ming Lee *[1,2,]**

[1] Division of Genomic Sciences and Cancer, The John Curtin School of Medical Research, The Australian National University, Canberra, ACT 2601, Australia

[2] ACRF INCITe Centre - ANU Node, The John Curtin School of Medical Research, The Australian National University, Canberra, ACT 2601, Australia

Address for correspondence

Dr W M Lee

The Australian National University,

Canberra ACT 2601, Australia

*Email: steve.lee@anu.edu.au

# Methods and sample preparation

## A. Dual camera detection for a single azimuthal scanning- oblique illuminated beam

The imaging system is constructed on an inverted microscopy platform (RAMM, ASI) using a linearly polarized 488 nm laser (Stradus 488-150), as shown in Fig. S1. A two-axis galvo mirror (GVS212/M, Thorlabs) is conjugated to the imaging plane of the system so that the laser beam is focused on the back focal plane of the objective lens (Olympus, 60X, NA 1.49, oil immersion) to allow wide-field illumination. The fluorescence and scattering signal is separated using a dichroic mirror (FF505-SDi01-25x36, Semrock) and collected by a CCD (Retiga 4000R, QImaging) and a sCMOS (PCO edge 4.2), respectively. To achieve oblique illumination and azimuthal averaging, a galvo mirror (GVS212/M, Thorlabs) was used to radically scan around the optical axis at the back focal plane of the objective. We also synchronized the capture rate of the sCMOS and the scanning frequency with a data acquisition card (PCIe-6374, National Instruments) so that one complete cycle of an azimuthal scan can be captured and averaged simultaneously. The laser on/off trigger was also synchronized with the scanning frequency to create a pulsed illumination and reduce photobleaching (see Fig. S5).

The switching between interference signal and pure scattering detection is achieved through tailoring the oblique illumination angle by controlling the scan radius at the BFP of the objective and Fourier amplitude filtering by placing a diaphragm (Thorlabs, ID15/M) at the Fourier plane (conjugated to the back focal plane of the objective) as shown in Fig. S1. The diaphragm modifies the BFP aperture and the detection N.A. of the scattering detection (N.A. = 1.27, illumination angle = 57°) so that the back reflection can be blocked to collect pure scattering signal. The detection N.A. of the fluorescence signal is not limited by the diaphragm and will always be equal to the N.A. of the objective (1.49) at various oblique illumination angle as shown in Fig. S1. Fig. 1B (iv-vi) illustrates the fluorescence signal from F-actin of the fixed fibroblast cell at an angle of 22.7°, 60° (HiLo) and 63° (TIRF) respectively. With increased oblique illumination angle, imaging depth of field is also reduced.

## B. Determination of illumination angle

The scan radius at the back focal plane of the objective is firstly measured by recording the position of the back-reflected beam at the conjugation. Fig. S4A and 4B demonstrated the maximum intensity projection of the reflected beam at various illumination angles at oil-air and oil-water interfaces. The sudden jump in reflected intensity, indicates having reached a critical angle where most of the light was being reflected by the coverslip. The theoretical value of critical angle and maximum angle can be achieved by the objective can be calculated using Eq. 1 and 2, where $\theta_{max}$ =78.98° and $\theta_{critical}$ = 61.4° and 41.2° for oil-air and oil-water interfaces. Those values and the measured radius are then substituted into Eq. 3 for calculating illumination angle θ. The plot of galvo voltage and scan radius is shown in Fig. S4C, while the scan radius corresponding to the illumination angle is shown in Fig. S4D.

$$\theta_{critical} = \arcsin\left(\frac{n_2}{n_1}\right) \quad (1)$$

$$\theta_{maximum} = \arcsin\left(\frac{NA}{n_2}\right) \quad (2)$$

$$r = f_{obj} n_1 sin\theta \quad (3)$$

## C. Quantification of signal to noise ratio (SNR)

The foundation of interferometric scattering signal ($I_{det}$) lies in three components: namely back-reflection intensity; known as reference field ($I_r = |\overline{E_r}|^2$) pure scattering field ($I_s = |\overline{E_s}|^2$) known as sample field in ROCS [22], and the superposition of reference and scattering ($2E_rE_s\cos\phi$, wherein $\phi = \phi_r - \phi_s$ are the relative phase difference between sample and reference) that refers to interferometric scattering [41, 44].

$$I_{det} \propto |\overline{E_r} + \overline{E_s}|^2 = I_r + I_s + 2E_rE_s cos\phi \quad (4)$$

For nanoscale imaging, scattered intensity ($E_s$) is a few folds (~x) lower than the reference intensity ($E_r$). The superpositioning of the reference and sample amplitude $E_rE_s$ would be imbalanced, resulting in poor interference visibility. To access interferometric scattering, it is crucial to ensure that the superposition intensity $2E_rE_s\cos\phi$ is not being masked by a dominant reference field ($I_r = |\overline{E_r}|^2$).

The gold/polystyrene particles were firstly diluted to desired concentrations using distilled water and dried on a no.1 coverslip. Prior to an imaging session, a drop of distilled water (100 µL) was added to the nanoparticles adhered onto a coverslip via Van Der Waals forces. To calculate the SNR of the nanoparticles at a specific illumination angle, a minimum of 50 regions containing single particles were cropped from the original image, captured by the camera. The peak value and averaged background were used for computing SNR using Eq. 5 and outliers (beyond ± 1.5*std) were removed.

$$SNR = \frac{abs(I_s - I_{bkg})}{I_{bkg}} \quad (5)$$

## D. Fixation and staining of fibroblast cell

An L929 murine fibroblast cell line was maintained in Dulbecco's modified Eagle's medium containing 10% fetal bovine serum in a humidified 10% CO2 atmosphere at 37 °C. Before each experiment, cells were re-plated onto custom-made polydimethylsiloxane (PDMS) imaging chambers and grown for an additional 1−2 days until a confluency of ~70% coverage was reached. Cells were fixed with 4% paraformaldehyde (Thermo Scientific) in PBS for 15 minutes, followed by three PBS washes and then permeabilized with 0.1% Triton X-100 for 15 minutes. Permeabilized cells were washed with PBS three times and then incubated with Alexa Fluor 488 conjugated phalloidin (Actin Green 488 ReadyProbes, Invitrogen) for 30 minutes to visualize intracellular actin followed by three PBS washes before imaging.

## E. Isolation and preparation of human platelet

The protocol of isolation human platelets was adapted [4]. Venous whole blood was collected in acid-citrate-dextrose (ACD; 97 mM trisodium citrate, 111 mM glucose, 78 mM citric acid). To obtain washed platelets, whole blood was firstly diluted 1:1 with modified Tyrode's buffer (137 mM NaCl, 2.8 mM KCl, 12 mM $NaHCO_3$, 5.5 mM glucose, 10mM HEPES, pH 6.5) and centrifuged at 70 g for 30 min at room temperature with no brake. The supernatant containing platelet rich plasma (PRP) was diluted 1:3 parts with modified Tyrode's buffer containing 0.1 µg/ml $PGI_2$ (Abcam) and centrifuged at 1250 g for 10 min at room temperature (RT). The pellet was then re-suspended in modified Tyrode's buffer (with adjusted pH 7.4) to achieve a platelet concentration of $5 \times 10^8$ platelets/mL.

## F. Fibrinogen/fibrin coating

The fibrinogen/fibrin coating protocol is adapted and modified [4]. Coverslips (#1) was firstly immersed in 20% $NHO_3$ for 1 hour and washed with distilled water (ddH2O). The acid-washed coverslips were then immersed in ddH2O for another hour and rinsed again with $ddH_2O$. The cleaned coverslips were then dried on a coverslip rack. Before fibrin/fibrinogen coating, a layer of HMDS was silanised on the coverslip by vapor deposition to create a hydrophobic surface for protein binding. The dried coverslips were plasma cleaned for 4 minutes and then placed in a vacuum desiccator together with a vial containing 1 ml of HMDS solution at room temperature. The desiccator was connected to a vacuum pump in a fume hood to deposit the HMDS vapor for 40 minutes. The effectiveness of HMDS coating is verified by checking the contact angle of the surface.

After the HMDS coating, a customized PDMS chamber (radius 10 mm, depth 6mm) was placed on the coverslip and 200 ul fibrin (300 μg/ml fibrinogen, 12 mg/ml BSA, 2U/ml thrombin, and 1 mM $CaCl_2$ supplemented in modified Tyrode's buffer, pH=7.4) or fibrinogen solution (300 μg/ml fibrinogen and 12 mg/ml BSA supplemented in modified Tyrode's buffer) was loaded into the chamber. These solutions were used immediately after mixing. For control experiments, modified Tyrode's buffer (pH=7.4) is added instead of BSA. The fibrin and fibrinogen coverslips were coated for 30 minutes and 1 hour at room temperature, respectively and then washed with modified Tyrode's buffer (pH=7.4) three times before use.

## G. Platelet migration

Washed platelets was supplemented in modified Tyrode's buffer (pH=7.4) with 1 mg/ml BSA, 200 μM CaCl2, 4μM U46619 and 10 μM ADP at final concentration of 107 platelets/ml. The imaging chamber was incubated at 37 °C for 40 minutes to allow platelet adhesion and migration before imaging. Note that incubation at 37 °C is recommended but not a determinant factor for migration. Platelet migration is also observed at room temperature but at a much slower speed and shorter trajectory.

## H. Morphological profiling of single platelet during migration

The processing of quantifying morphological features is illustrated in Fig. S5. The fluorescence and scattering images are firstly overlapped to recognize migrating platelets. The criteria we used to check if a platelet is migrating is to confirm if there is a dark region associated with the platelet. The area of the dark region needs to be larger than half of a platelet size. We then cropped scattering images of the migrating and non-migrating platelets into a small field of views (500×500 pixels) using Fiji (ImageJ). We put them into a different group for shape analysis using a Cell profiler. The total number of platelets being processed is 937, including 427 on fibrin surface (288 platelets with BSA, 139 without BSA) and 510 on fibrinogen surface (318 platelets with BSA, 192 without BSA). To generate binary segmentation of the platelets, the following modules are used in the processing: rescale intensity, identify primary object (platelet, with adaptive threshold, otsu method), identify secondary object (filopodia associated with the identified platelet, adaptive threshold, robust background method). The processed data is reviewed and edited manually if two objects touch each other. Morphological features of the platelet are calculated using "measure object size and shape" module in the Cell profiler. As shown in Fig. S5C, the area is calculated as the product of the number of pixels covered in the object and the actual pixel size of the imaging system (0.025 $\mu m^2$/pixel). The convex area is the area of the convex hull that encloses the object, and the

solidity is defined as the object area/convex area. In Fig. S5C, we demonstrated the filopodia rich shape platelet can have a solidity of 0.39-0.7 while the round or half-moon shape platelets is around 0.85-0.94.

### I. Tracking intensity along lamellipodia during platelet migration

To track the intensity on the lamellipodia of the platelet, a binary mask showing only the edge of the platelet was firstly generated based on the scattering signal using ImageJ (auto local threshold function with Nilblack algorithm and radius = 8). As the membrane ruffles during migration and causes lamellipodia shifts in the lateral position, a stack of binary masks that corresponds to the lateral part of the edge at a different time point is generated to filter the intensity at lamellipodia only. After that, 14 regions on the lamellipodia were manually selected in the binarized image and then converted to ROIs using the BIOP image analysis plugin. The ROIs were then selected on the interference image to quantify mean intensity. Because of varying intensity in scattered signals, the cell outline might appear discontinuous in some frames after binarization and creating multiple small ROIs in one frame, a separate MATLAB script is used to re-calculate mean intensity when multiple ROIs were presented.

### J. Live endothelial cell culture and imaging

Human microvascular endothelial cell line (HMEC-1, CRL-3243, ATCC) and were maintained in MCDB131 medium (Invitrogen) supplemented 10% heat-inactivated fetal bovine serum (Sigma), 5 U/ml of penicillin, streptomycin and neomycin (Invitrogen), 2 mM of L-glutamine (Invitrogen), 10 ng/mL epidermal growth factor (Invitrogen) and 1 μg/ml of hydrocortisone (Sigma). Primary human microvascular cells derived from the lung (HMVEC, Lonza) were maintained in EGM2-MV2 Bulletkit (Lonza). At 37°C and 5% CO2. For imaging experiments, HMVEC cells were seeded onto glass bottom dishes (ibidi) at a concentration of $2.5 \times 10^4$ cells/mL coated with Poly-L-Lysine (PLL) for 30 minutes and incubated at 37°C for 24 hours before imaging. Cells were stained for 30 minutes with Mitotracker Green FM (100 ng/mL, Invitrogen) prior to imaging and kept on a heat plate (37°C) during imaging.

### K. Segmentation of mitochondria

Segmentation was performed on fluorescence video using the MATLAB software Mitometer [71] using the 2D analysis function and omitting fission and fusion events. The segmentation masks were exported from Mitometer and thresholded in Fiji to select the mask. The selection was then exported as region of interests (ROI) using the Analyze Particles function. The ROIs were applied to the scattering or interference videos and all signal outside of the ROIs were cleared.

# Supplementary figures

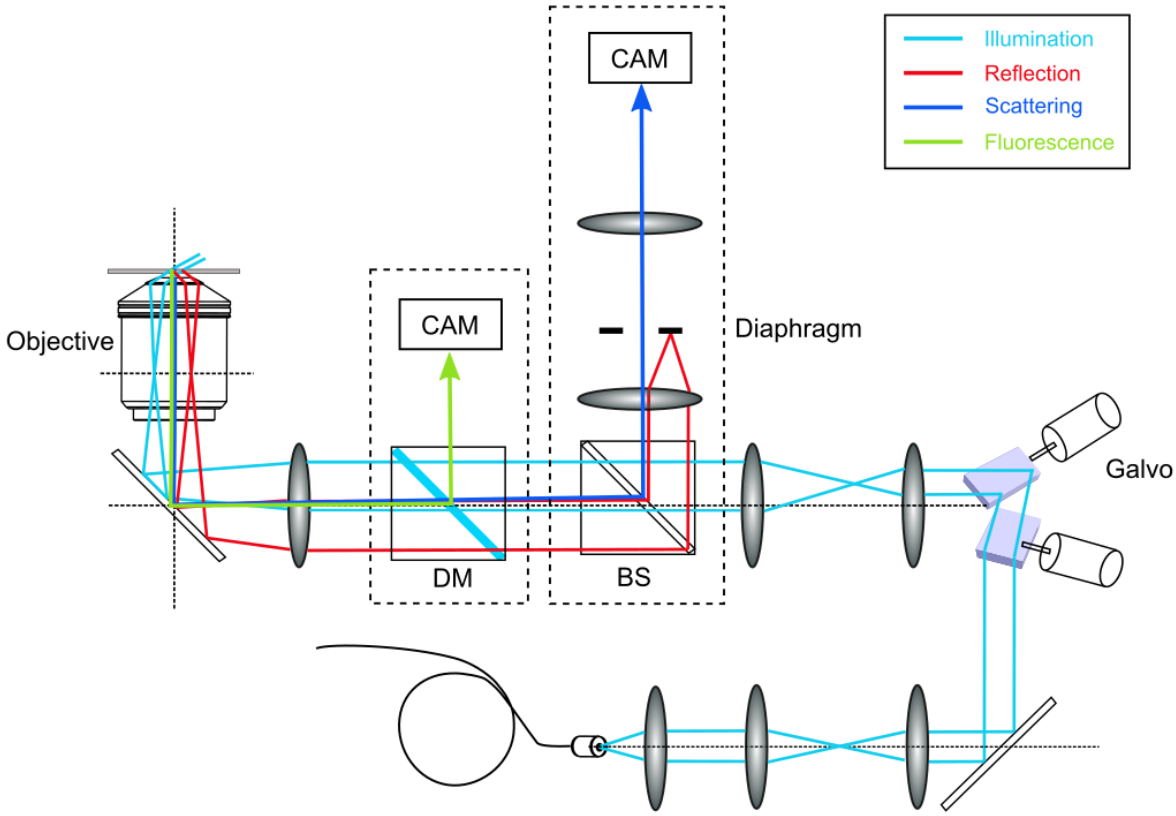


**Fig. S1 Optical setup of combined scattering, interference and fluorescence imaging system.** The imaging system is constructed on an inverted microscopy platform (RAMM, ASI) using a single laser source (Stradus 488-150). A two-axis galvo mirror (GVS212/M, Thorlabs) focuses the laser beam onto the back focal plane of the objective lens (Olympus, 60X, NA 1.49, oil immersion), and project radical scanning pattern that allows oblique illumination and azimuthal scanning. The fluorescence and scattering signal are separated using a dichroic mirror (FF505-SDi01-25x36, Semrock) and collected by a CCD (Retiga 4000R, QImaging) and a sCOMS (PCO edge 4.2) respectively.

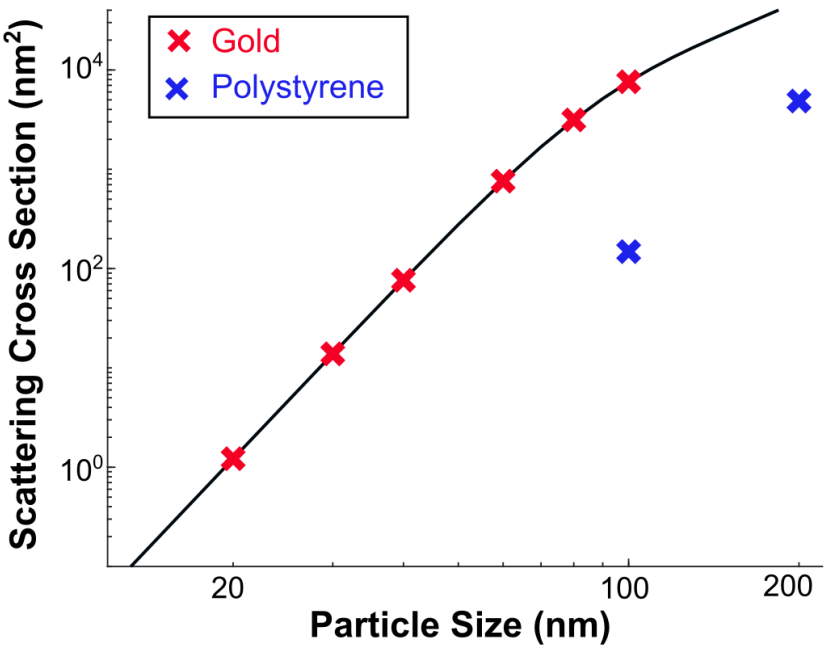


**Fig. S2 Scattering cross section of gold (20 nm, 30 nm, 40nm, 60nm, 80 nm and 100 nm) and polystyrene particles (100 nm and 200 nm), calculating using Mie theory.** The calculation of scattering cross section is based on illumination wavelength of 488 nm, refractive index of the medium and particles to be 1.33, 1.1271+1.8382i (gold) and 1.59 (polystyrene) respectively. The plot is in log-log scale.

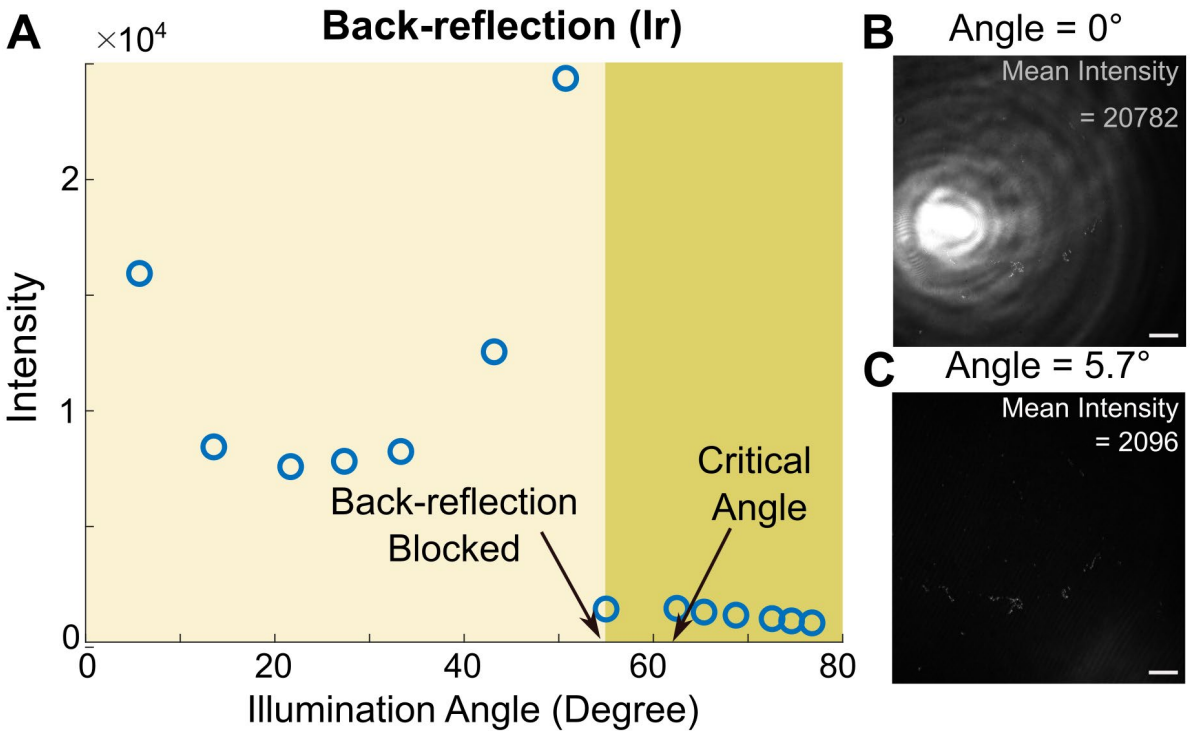


**Fig. S3 Measurement of back-reflection intensity from the coverslip. (A)** Plotting of back-reflection meaning intensity at various illumination angle (5° to 76°). The intensity is measured by capturing reflected light of an empty coverslip covered with water (refractive index = 1.33) at fixed exposure of 30 ms. Example of back-reflection signal and calculated mean intensity with **(B)** on-axis illumination (θ = 0°) and (B) oblique illumination (θ = 5.7°), measured at exposure of 5 ms. Scale bar = 10 μm

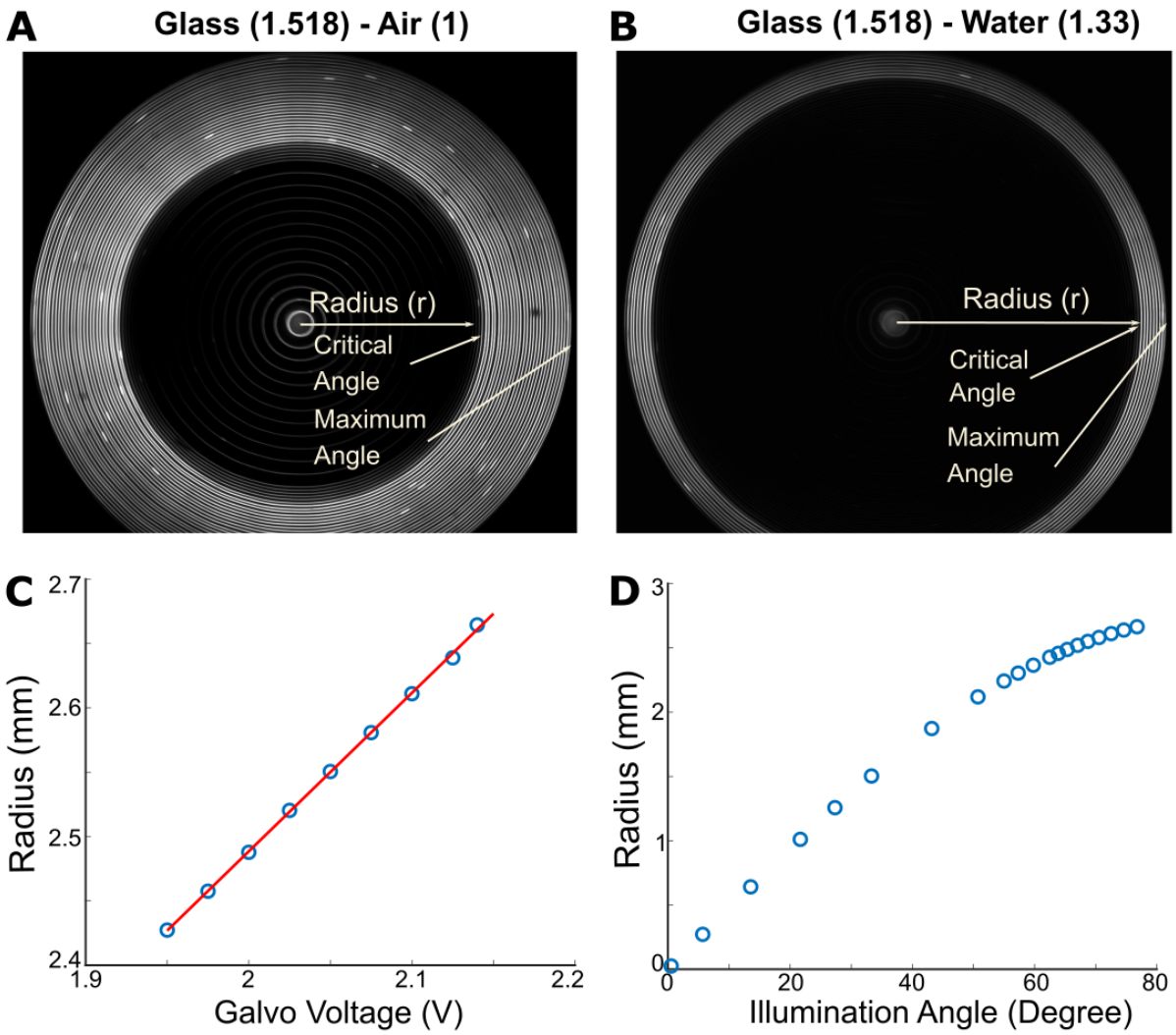


**Fig. S4 Measuring oblique illumination angle.** Recording of the reflected light at back focal plane of two different mediums (A) air (refractive index = 1) and (B) water (refractive index = 1.33) (C) Plotting of measured scanning radius and galvo voltage. Red line shows the fitted linear relation between radius and voltage. (D) Plotting of calculated the illumination angle vs. scanning radius.

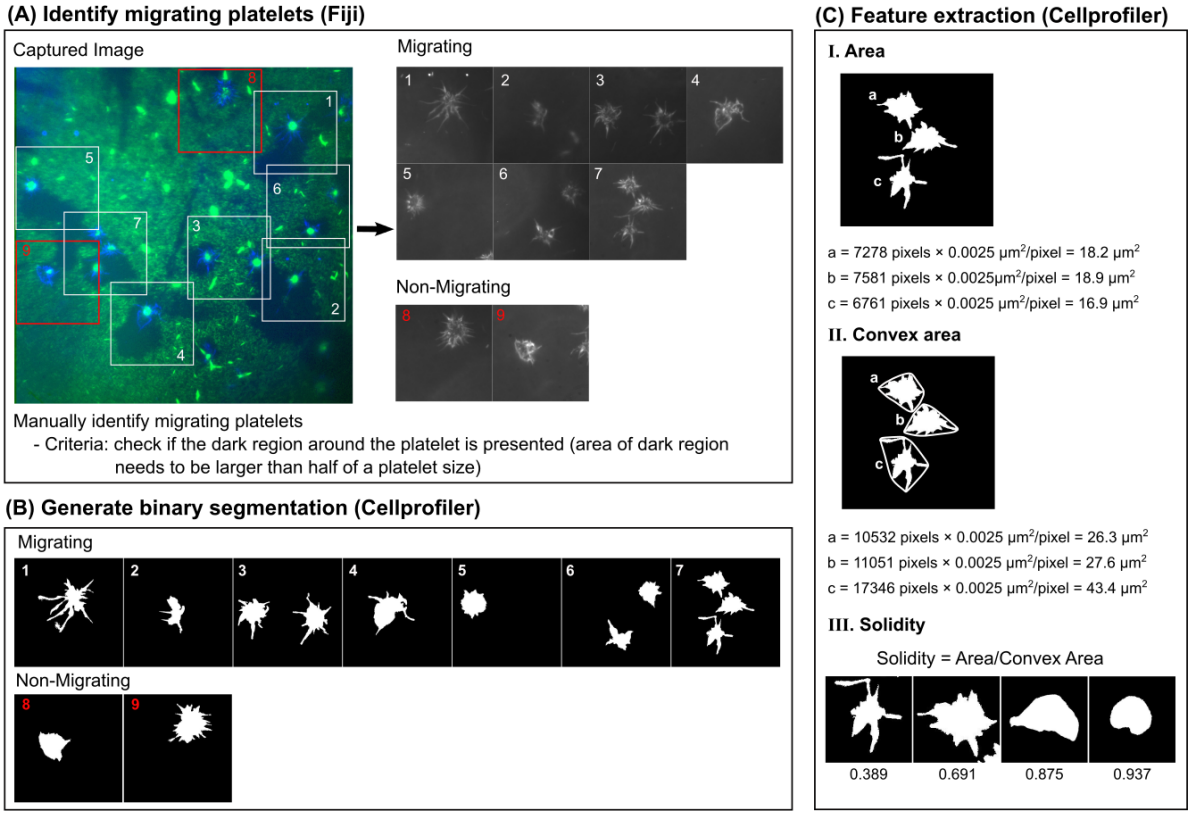


**Fig. S5 Quantifying morphological features of platelets using Fiji (ImageJ) and *Cell profiler*. (A)** The migrating platelets are firstly identified manually using the overlapping image of fluorescence (green) and scattering (blue) signal. The criteria for migration is to check if there is a dark region associated with the platelet and the area of the dark region needs to be larger than half of a platelet size. The migrating and non-migrating platelets are then cropped into small field of views (500×500 pixels) and put into different group for shape analysis. (B) After that, the binary segmentation is generated using cell profiler and the morphological features (area, convex area and solidity) are calculated. (C) These quantifications are illustrated and explained with examples.

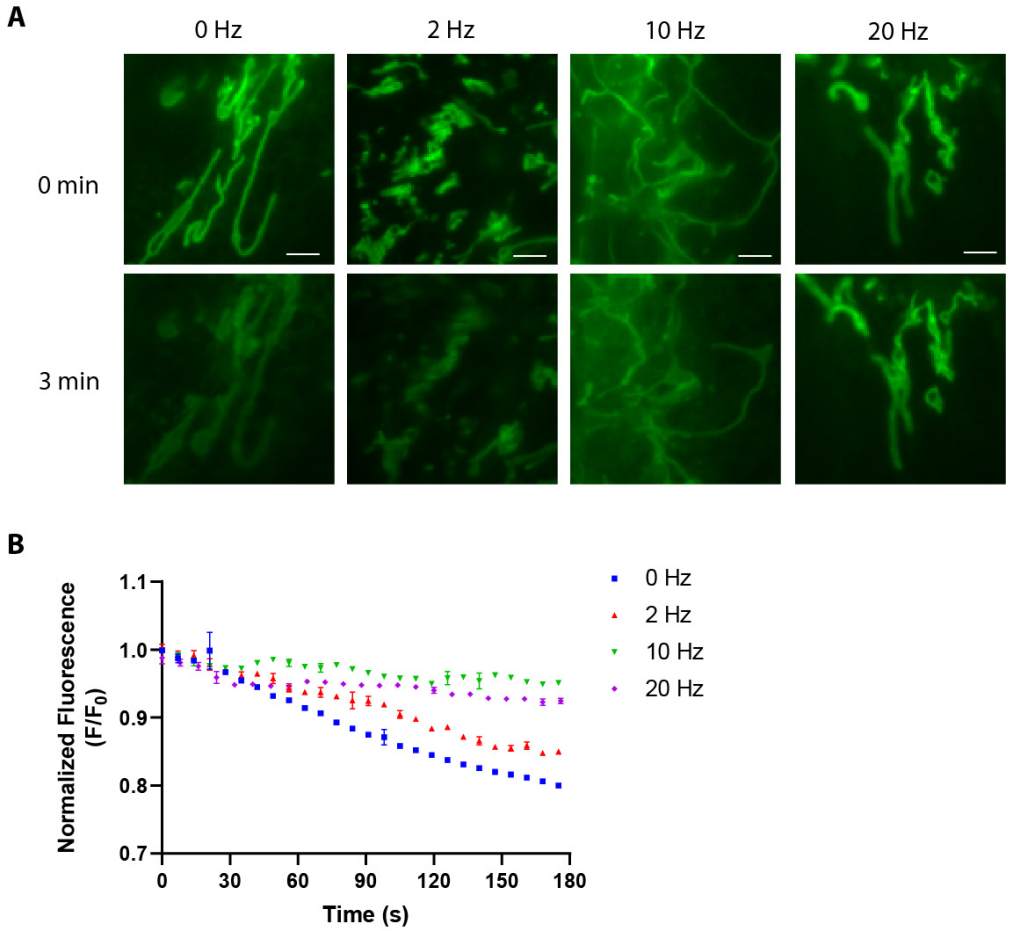


**Fig. S6. Reducing photobleaching with laser pulsing.** (A) Fluorescence imaging of primary human endothelial cells stained with Mitotracker Green before and after 3 min illumination with 0 – 20 Hz laser pulse. (B) Plot of Mitotracker fluorescence in measured in (A), normalized to intensity at start of imaging and plotted over illumination time. Intensity values are the average of 5 frames.

**Movie 1**- Simultaneous recording of both scattering and interference of single platelet spreading on fibrin coated surface

**Movie 2** - Video recording of leading edge of filopodia of a single platelet being folded into a leading lamellipodium after adhesion on fibrin surface

**Movie 3** –Interference, scattering and fluorescence imaging of a single platelet migrating on fibrin coated surface.

**Movie 4** – Automated tracking of platelet interference images along the boundaries during migrating (highlighted in green) on fibrin surface. The boundaries are segmented using auto local threshold function with Nilblack algorithm in ImageJ.

**Movie 5** – A single sub-region tracking (highlighted in green) on the rear edge of interference images of platelet migrating on fibrin surface using ImageJ.

**Movie 6** – Real time interference, scattering and fluorescence imaging of migrating live HMEC-1 endothelial cells labelled with Mitotracker Green. Mitochondria were segmented using the Mitotracker fluorescence signal. Videos of expanded FOVs show real-time axial and lateral motion of mitochondria and membrane retrograde flow at the cell's leading edge.

**Movie 7** – Interference and fluorescence imaging of a migrating HMEC-1 cell stained with Mitotracker Green. Highlighted sections show interference imaging of membrane retrograde movement at the cell leading edge and fluorescence imaging of mitochondria lateral motion. Expanded video reveals time point when a mitochondrion enters the nucleus.